

Available online at www.sciencedirect.com

ScienceDirect

Energy Procedia 92 (2016) 531 – 539

Energy

Procedia

6th International Conference on Silicon Photovoltaics, SiliconPV 2016

Optimizing the solar cell front side metallization and the cell interconnection for high module power output

Robert Witteck^{a,*}, Henning Schulte-Huxel^a, Hendrik Holst, David Hinken^a, Malte Vogt^a,
Susanne Blankemeyer^a, Marc Köntges^a, Karsten Bothe^a, and Rolf Brendel^{a,b}

^aInstitute for Solar Energy Research Hamelin (ISFH), Am Ohrberg 1, 31860 Emmerthal, Germany

^bDep. Solar Energy, Institute for Solid State Physics, Leibniz Universität Hannover, Appelstraße 2, 30167 Hannover, Germany

Abstract

Improving the light trapping in a module results in an increase in the generated current. Consequently, an optimization of the front grid metallization of the cell is required for the best trade-off between series resistance, shading, and recombination losses. For this purpose, we combine ray tracing and electrical solar cell and module calculations that explicitly account for cell and module interactions. Our model bases on experimentally verified input parameters: We determine the electrical and optical properties of the front metal fingers of passivated emitter and rear cells (PERC). We show that the effective optical width of the front metal fingers in the module is significantly reduced by 54%. The optimized simulated module has 120 half-size PERC with 20.2% cell efficiency and has an output power of 295.2 W. This is achieved with an increased number of 120 front metal fingers per cell, four white-colored cell interconnection ribbons (CIR), and an increased cell spacing. Applying these optimized design changes to an experimental module we measure a module power output of 294.8 W and a cell-to-module (CTM) factor of 1.02. Measured and simulated power agree and the deviations in V_{oc} , I_{sc} and FF are less than 0.91%_{rel}. We perform a module power gain analysis for the fabricated module and simulate a potential maximum module power of 374.1 W when including further improvements.

© 2016 The Authors. Published by Elsevier Ltd. This is an open access article under the CC BY-NC-ND license (<http://creativecommons.org/licenses/by-nc-nd/4.0/>).

Peer review by the scientific conference committee of SiliconPV 2016 under responsibility of PSE AG.

Keywords: Solar modules; front metallization; cell interconnection; cell to module losses; PERC solar cells

* Corresponding author. Tel.: +49 5151 999 429; fax: +49 5151 999 400.
E-mail address: witteck@isfh.de

1. Introduction

Transferring solar cells into a module comes in general along with cell to module (CTM) losses due additional series resistance contributions by the cell interconnection and optical losses caused by the encapsulation. Several publications have dealt with this topic in the past [1] [2] [3] and showed that analytical modeling allows to break down the optical and electrical power losses. However, the interaction of the cell design and module design is often neglected. Here we show, that optimizing cell and module design together leads to a modified cell front metallization. This contribution focuses on the front side metal fingers of the cells in the module. We measure their geometrical, optical and resistive properties and quantify their impact on the recombination behavior of the cell. We determine their effective optical widths when operating in a module. With these data we perform cell and module simulations applying an analytical model [4] that considers the optical interaction of cell and module components and includes resistive and recombination effects.

Then we produce a batch of solar cells according to the optimization results and manufacture a module consisting out of 120 half-cell solar cells to compare modelling and experiment. Finally, we perform a synergistic gain analysis to elucidate further conceivable optimization potentials to improve the module power output.

2. Cell production and characterization

We produce a batch of PERC solar cells following the process given in Ref [5] to determine necessary input parameters for our model. The front metallization of the cells consists out of 88 front metal fingers and 3 busbars. We measure the dark IV , J_{sc} - V_{oc} , and the illuminate IV -curves for each cell and fit the measurement data with the double-diode model. We extract the diode saturation current densities J_{01} and J_{02} . For the surface recombination of passivated and metallized areas we use data given in Ref. [5] and [6]. With this we calculate the contribution to the J_{01} by the front and the rear side from the sum of the area-weighted passivated and metallized regions. Passivated and metallized areas are denoted as the emitter and the front metallization for the front side and are denoted the silicon nitride (SiN) and laser contact openings (LCO) at the rear side, respectively. The difference between the measured J_{01} and the calculated contributions from both surfaces is assigned to originate from base recombination. We thus assume that j_{02} is not affected when changing the metallization pattern.

For determining the contact area of the front metallization we measure the width w and thickness t of the fingers ($w_f = 60 \mu\text{m}$, $t_f = 18 \mu\text{m}$) and busbars ($w_{bb} = 1 \text{mm}$, $t_{bb} = 12 \mu\text{m}$) with a scanning electron microscope (SEM) and a profilometer, respectively. Figure 1 shows an SEM cross section image of a front metal finger. The overlaying plot serves as a measure for w_f and t_f , while the red plot is a fit to the profile of the finger.

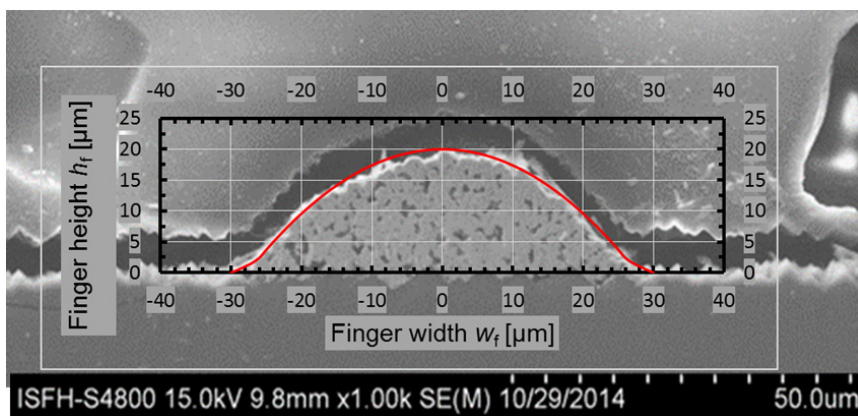


Fig. 1: Scanning electron image of the cross section of a front metal finger. The graph shows the function we applied to fit the finger profile.

One cell of the batch is sliced into 1 cm narrow stripes in the direction perpendicular to the fingers. The stripes serve for determining the contact resistance of the metal paste with the transmission line method (TLM). We use a TLM system (TLM-SCAN+, *pytools*), which generates a series resistance mapping. The mean contact resistance is measured to be $8 \text{ m}\Omega\text{cm}^2$. For the busbars we assume the same contact resistance since we use single printing technology. We determine the resistivity of the front metal fingers and busbars to be $3.15 \text{ }\mu\Omega\text{cm}$ employing four-point probe measurements.

We measure the external quantum efficiency (EQE) and the reflection of the $156 \times 156 \text{ cm}^2$ -large cells with a $2 \times 2 \text{ cm}^2$ light spot in an area that does not contain busbars. The reflection is measured with an integrating sphere. We also print a full $2 \text{ cm} \times 2 \text{ cm}$ area of the silver metallization paste on a test cell to measure the reflection of the metallization paste. Fig. 2 shows the measured reflectance $R_{Ag}(\lambda)$ of the Ag paste and the reflectance $R_{tot}(\lambda)$ of the cell area with fingers.

With the reflection data of the silver paste and the cell we determine the effective optical width of the fingers [7] [8]. The total measured reflection of the cell $R_{tot}(\lambda)$ comprises the reflection of the metal fingers $R_{Ag}(\lambda)$ and the silicon with the anti-reflection coating (ARC) in the intermediate area in-between the fingers $R_{int.}(\lambda)$

$$R_{tot}(\lambda) = \mu R_{Ag}(\lambda) + (1 - \mu) R_{int.}(\lambda), \quad (1)$$

where μ is the effective optical fraction of the front metallization. Assuming that due to the ARC the minimum reflection of the intermediate area $R_{int.}(\lambda)$ is approximately zero at a certain wavelength λ_0 , we attribute the remaining reflection to the front side metallization and can determine μ . Since μ is constant for all wavelengths using Eq. (1) we determine $R_{int.}(\lambda)$. We need to iterate this procedure until μ converges, since the minimum of $R_{tot}(\lambda)$ and $R_{int.}(\lambda)$ are not necessary found for the same λ_0 due to the wavelength dependence of R_{Ag} . Solving the minimization problem we determine the corrected reflection (Fig. 1 green curve) and the optical effective metallization fraction of the fingers.

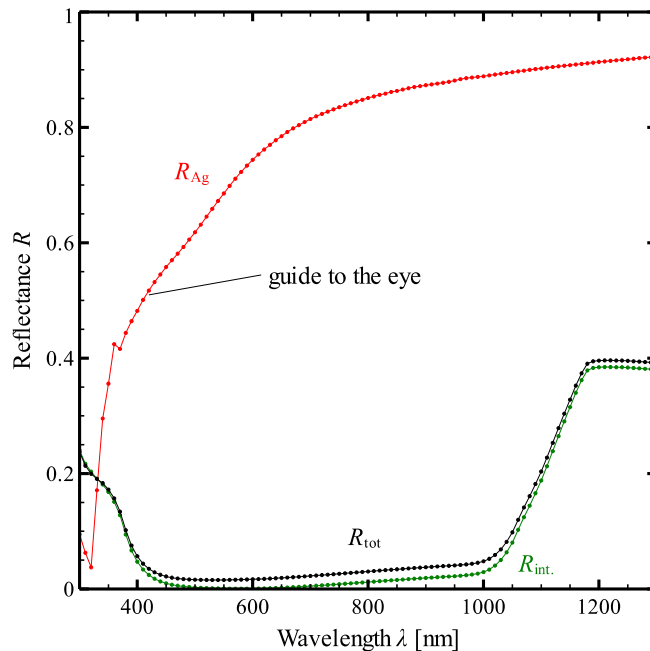


Fig. 2: The symbols show reflectance measurements of the Ag paste on the front side and the reflectance of the cell with printed fingers. The black curve shows the reflection data of the initial cell measurement and the green curve shows the reflection of a cell without front side metallization as determined by equation (1).

From the reflection measurement in Fig. 2 and the deduced fraction of the front metallization μ , we determine the effective optical width of a front metal finger for a cell in air. The geometrical fraction of the metallization is determined by the geometrical finger length $l_{f,geo}$ and width $w_{f,geo}$. Since we know the number of front metal fingers within the light spot that measures the reflection we can calculate the effective optical width of one finger $w_{f,eff}$ from the metallization fraction. We introduce an optical factor k_f as the ration between the effective optical and the geometrical width of a finger

$$k_f = \frac{w_{f,eff}}{w_{f,geo}} = \frac{\mu p_f}{w_{f,geo}}, \quad (2)$$

where p_f is the pitch of the fingers. We determine the optical reduction factor for the front metal fingers of a cell in air $k_{f,cell}$ to be in the range of 0.87 to 0.91. The factor varies, since the shape of the fingers varies in different areas of the cell.

3. Optical cell and module simulations

In section 2 we deduce the optical reduction factor for a cell in air from reflection measurements. However, in a module, photons reflected by the fingers and the cell may be total internal reflected at the glass-air interface and hence, can travel long distances due to multiple reflections. This is challenging for the measurement aperture, since not all the light of the measurement spot may be reflected back into the integrating sphere. Thus, we employ our in-house-developed ray tracer *Daidalos* [9] to determine an optical reduction factor for the fingers of a cell within a module $k_{f,mod}$.

The ray tracing software is based on a multi-domain approach and hence, allows simulating the complete module including cell texture, fingers, ethylene vinyl acetate (EVA), glass, anti-reflection coatings and the backsheet. The optical data are taken from Refs. [10], [11] and [12]. From the ray tracing simulation we obtain a short circuit current density J_{sc} of the simulated domain.

First, we simulate a cell in air according to our measurements. We simulate an area A_0 that is infinite in the direction perpendicular to the fingers and has a width that is similar to the distance between the front metal fingers of the measured cell. We employ periodic boundary conditions in the latter direction. This simulation only comprises the cell without any front metallization. Then we perform a second simulation of the same area, but including one front metal finger and therefore denoted as A_{act+f} . For the finger we apply the function of the profile in Fig. 1 and assume a uniform spatial expansion of the profile in the length dimension of the simulation area. However, the measurement results in section 2 revealed that the shape of is rather inhomogeneous. This non-uniformities are considered with a Lambertian factor \mathcal{A} . If $\mathcal{A}=0$ the finger is reflecting specular and $\mathcal{A}=1$ assumes that the finger is a perfect diffuse Lambertian reflector.

Let A_{act+f} consist out of an active area A_{act} , which contains no front metal fingers and an area A_f , which represents the area shaded by the fingers. We assume a homogenous current generation for the two simulation and that the generated current density for the active cell area A_{act} is equal to the generated current density for A_0 , which comprises only active cell area. Thus, we can calculate the effective optical area of the finger by

$$\frac{I_{sc}(A_0)}{A_0} = \frac{I_{sc}(A_{act+f})}{A_{act}} = \frac{I_{sc}(A_{act+f})}{A_{act+f} - A_f} \Rightarrow A_f = A_{act+f} - \frac{I_{sc}(A_{act+f})}{I_{sc}(A_0)} A_0. \quad (3)$$

Thus, applying Eq.(2) we can determine the optical factor for the finger $k_{f,cell}$ from the simulation.

Then we do the same simulations for a cell in a module and calculate the optical factor $k_{f,mod}$.

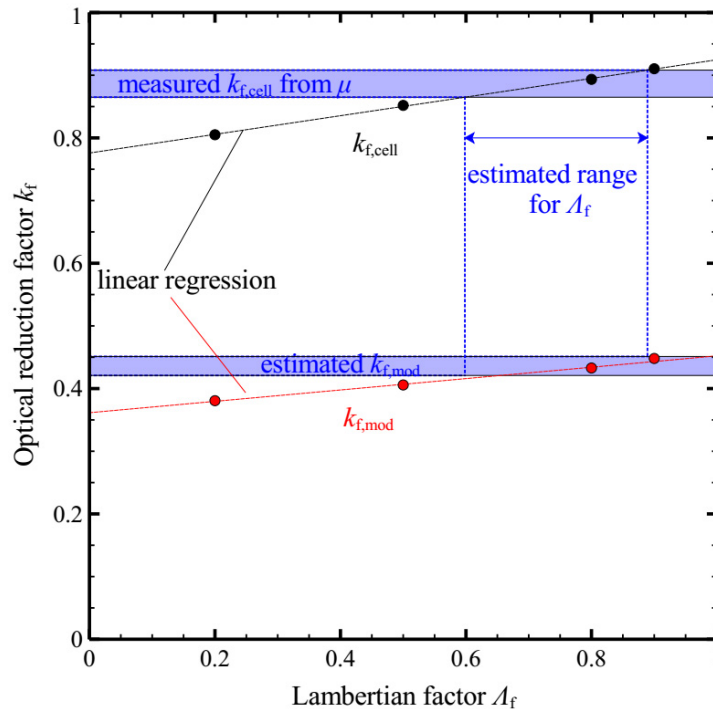


Fig. 3: Optical factor for the front metal fingers for different Lambert factors. We distinguish between finger on a cell in air $k_{f,cell}$ and on a cell in a module $k_{f,mod}$. The dashed lines represent the linear regression. The dotted lines show how we deduce the Lambertian factor from the measurements and determine the optical factor for a cell in a module.

In Fig. 3 the simulated optical reduction factor of the fingers for a cell in air (black dots) and within a module (red dots) is shown for various Lambertian factors. The dashed lines represent the linear regression fit. The blue dotted lines indicate the range of the measured optical factor for a cell in air from section 2. From the measurement results for a cell in air and the simulations we can deduce the optical factor for the fingers within a module, as it is indicated by the blue dotted lines in Fig. 3. Here, we assume that the Lambertian factor A_f is not influenced by the encapsulation.

Due to the parabola like shape of the finger, it is advantageous if the reflection behavior is more specular as most of the light, which impinges under normal incidence, is then directly reflected from the finger to the cell. If the Lambertian factor increases the finger reflects more diffusively and an increasing fraction of the light is scattered away from the cell ($k_{f,cell}$ increases).

Within a module the light scattered away from the cell may be reflected at the glass-air interface and hence, can contribute to the current generation. Thus, the effective optical width is significantly reduced within a module resulting in optical factors $k_{f,mod}$ between 0.42 and 0.45, i.e. a finger of a geometrical width of $60 \mu\text{m}$ may be reduced to an effective optical width of $25 \mu\text{m}$ within a module. This agrees with values presented in Ref. [13]. Note that a specular reflecting surface can also be advantageous within a module, depending on the profile shape of the fingers.

4. Modelling and fabricating a high power module

After determining the optical, electrical and recombination characteristics of the cells in air and within a module, we apply an analytical model to simulate a module and optimize the front metallization for a maximized module power output. Our analytical model utilizes symmetries and splits the cell into various unit cells [14]. The number

and area of the unit cells depends on the front metallization design, i.e. on the number of fingers and busbars. Thus, using the parameters determined in section 2 for the passivated emitter and contact areas, we calculate influence on the J_{01} for changes in the front metallization. With the optical factors we account for optical effects by changing the number of fingers. The resistive power losses are calculated by tracing the current path through the emitter and the finger. Hence, recombination, optical and resistive losses are combined in the model and it is appropriate to find the optimal front metallization to maintain the balance of these losses.

For further details about the model and a complete list of further required parameters to simulate the complete module we refer to Ref. [4].

For the optimization of the front metallization regarding a maximized module power output we assume that the module uses half cells, a white colored backsheet and four cell interconnection ribbons per cell. Optimizing the number of fingers for this configuration and a module with cells in air results in 88 front metal fingers. This confirms that the number of fingers of our cells used in section 2 was optimized for a cell in air. The calculated module power is 293.5 W. Performing an optimization for a cell encapsulated in a module results in an increased number of 120 front metal fingers with a predicted slightly larger module power output of 295.2 W.

We produce a second similar batch of PERC cells. However, instead of three busbars and 88 front metal fingers the cells have four busbars and 120 fingers. Due to the smaller optical effective widths of fingers and ribbons in a module compared to cells in air as well as the reflection by the backsheet, the module current increases and more fingers are required to balance optical shading, recombination losses and resistive power losses. The cells are cut into halves prior to interconnecting them. Cutting the cells into halves reduces series resistance losses since the generated current decreases and resistive power losses scale with the current squared [15]. We apply white colored CIR since they showed good optical properties [4]. We increase the cell spacing within the module since here we aim for a high module power rather than a high module efficiency. Due to the white colored backsheet, light impinging on the gaps between the cells is totally internal reflected at the glass/air interface and can thus contribute to the module current. The size of the laminator that we use, limits the cell to cell spacing to a maximum value of 4.7 mm and for the distance between the strings to a maximum value of 12.8 mm (1680 mm \times 1030 mm aperture area).

Fig. 4 shows a photo of the in-house fabricated module with in-house fabricated PERC cells. Table 1 lists the measured cell and module parameters as well as the simulation results. We measure a module power of 294.8 W which is a CTM gain of 5.1 W. The measured power agrees with the simulated power. Deviations in V_{oc} , I_{sc} and FF are less than 0.91%_{rel.} and are thus within the uncertainty of our measurement equipment. We conclude that the accuracy of our model is sufficient to describe the cell to module process. The validated model may thus be used to analyze option for further improvements.

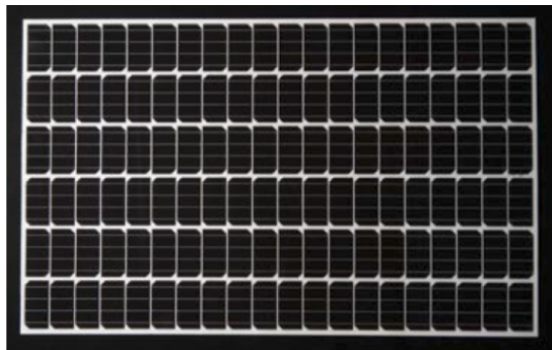


Fig. 4: Picture of the produced PERC module. The cell to cell spacing is 4.7 mm and the string to string spacing is 12.8 mm.

Table 1: Cell and module measurement and simulation

Type	V_{oc} (V)	I_{sc} (A)	FF (%)	P (W)	η (%)
Mean of cells	0.656	4.63	79.4	2.4	20.2
Sum of cells	78.7	-	-	289.7	-
Measured module	78.4	4.80	78.4	294.8	17.0
Simulation	79.11	4.76	79.1	295.2	17.1

5. Synergistic gain analysis for the 295 W module

Further improvements may be achieved by improving other parameters involved in the analytical model than those connected to the front metallization. Here we extend our gain analysis for solar cells [6] to modules. As for cells, we distinguish recombination, optical and resistive gains. Fig. 5 shows the simulation results of the synergistic gain analysis. The green bars denote optical, red bars recombination and blue bars resistive power gains.

We start with the simulation of the experimental module discussed above. It produces 295.2 W module and is represented by the left black bar in Fig. 5. It suffers from various optical, resistive and recombination losses. This is our reference simulation.

Then we disable one loss channel at a time in the simulation and calculate the corresponding module power enhancement. The gain in power compared to the reference is then added as a new bar in Fig. 5. For the next step this loss mechanism is enabled again and another loss mechanism is disabled.

Avoiding the extrinsic contribution of the base recombination and the rear side $j_{0,base}$ in the simulation, enhances the simulated power of the reference case by the length of the first red bar in Fig. 5. Then we re-enable these base and rear recombination losses and disable the reflection and the absorption losses in the glass cover. Following this procedure we stepwise disable the various loss mechanisms and sort them by the size of their gains. Accumulating the various power gains results in a maximum module power of 350.1 W. This power corresponds a module efficiency of 20.2% instead of 17.1% for the reference case. Note that we haven't adjusted the cell spacing in the simulation and the module area is fixed. If we could disable all power loss mechanisms simultaneously we obtained a maximum module power output of 374.1 W due to additional synergistic effects. In the gain analysis we assume a fixed short current density for the cell, which has to be considered for a theoretical module efficiency approaching the limit of 29%.

The gain analysis reveals that the biggest potential for an improved module is a reduction of the recombination in the base. The second largest improvement is from reducing the reflection and parasitic absorption in the glass. The series resistance losses (blue bar, emitter resist., 2.8 W) plays a minor role due to the improved front metallization. However, the shading by the front metal fingers (green bar, finger shading, 5.5 W) increases by using more fingers. According to the simulations results in Fig. 3 this loss channel can potentially be further reduced with specular reflecting fingers.

The contribution to the recombination at the front side metal contacts is 1.2 W (red bar, $j_{0,met}$).

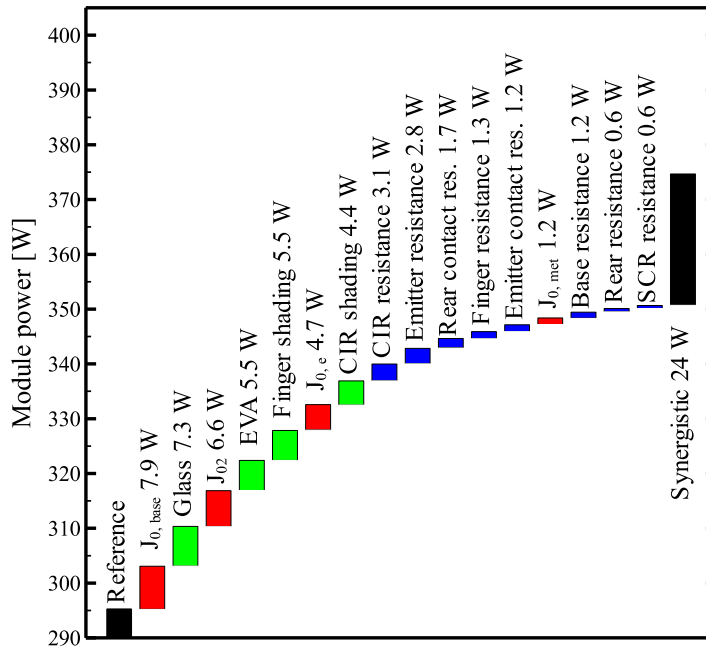


Fig. 5: Breakdown of the potential gain mechanisms of the 295 W module. We use green bars for optical, red bars for recombination and blue bars for resistive module power gains.

6. Conclusion

In this work we showed that the balance between recombination, optical and resistive effects is different for cells in air or in a module. Due to total internal reflection the effective optical width of the front metallization of the cell is reduced in a module. In addition, reflections from areas in-between the cell spacing result in an increased current generation within a module. Thus, an increased number of front metal fingers is required for optimum power output.

Analyzing reflection measurements we determined an optical reduction factor for cells in air in the range of 0.87 to 0.91. This measurement result was reproduced by ray tracing simulations and revealed that the finger reflection of the fingers is highly diffusive. We attributed this to the rough surface shown in Fig. 1. Using ray tracing we could determine a Lambertian factor for the screen-printed fingers in the range 0.6 to 0.89 and deduced an optical factor for the fingers within a module to be in the range of 0.42 to 0.45. The simulations show that the effective finger width reduces by 54%_{rel} in a module when compared to a cell in air.

The ray tracing simulations showed that a specular reflection characteristic is beneficial due to the shape of the fingers. A highly specular reflecting finger would reduce the effective optical width of the finger by 58% when assuming the measured finger shape shown in Fig. 1. Simulations for fingers that resemble a trapezoidal profile as it is typical for stencil print technology revealed an even stronger decrease of the optical width.

With our analytical model we accounted for the increased current generation and simulated the optimum number of fingers and busbars, which resulted in a power gain of 1.7 W compared to a module with a number of 88 fingers optimized for cells in air. We built a high power module following the simulation results and achieved an improved power output of 294.8 W. We found that the simulation and measurement agree within the measurement tolerance for voltage, current and power.

Acknowledgements

The results were generated in the PERC2Module project funded by German Federal Ministry for Economic Affairs and Energy under Contract 0325641. We would like thank the PERC2Module team for the cell and module production.

References

- [1] I. Haedrich, U. Eitner, M. Wiese und H. Wirth, „Unified methodology for determining CTM ratios: Systematic prediction of module power,“ *Solar Energy Materials and Solar Cells*, Bd. 131, Nr. 7, pp. 14-23, dec 2014.
- [2] A. Schneider, M. Pander, T. Korvenkangas, S. Aulehla, R. Harney und T. Hortana, „Cell To Module Loss Reduction and Module Reliability Enhancements By Solder,“ in 29th European Photovoltaic Solar Energy Conference and Exhibition, 2015.
- [3] M. Peters, S. Guo und Z. Liu, „Full loss analysis for a multicrystalline silicon wafer solar cell PV module at short-circuit conditions,“ *Progress in Photovoltaics: Research and Applications*, Bd. 20, Nr. 1, feb 2015.
- [4] R. Witteck, D. Hinken, H. Schulte-Huxel, M. R. Vogt, J. Muller, S. Blankemeyer, M. Kontges, K. Bothe und R. Brendel, „Optimized Interconnection of Passivated Emitter and Rear Cells by Experimentally Verified Modeling,“ *IEEE Journal of Photovoltaics*, pp. 1-8, 2016.
- [5] H. Hannebauer, M. Sommerfeld, J. Müller, T. Dullweber und R. Brendel, „Analysis of the Emitter Saturation Current Density of Industrial Type Silver Screen-Printed Front Contacts,“ 27th European Photovoltaic Solar Energy Conference and Exhibition, pp. 1360-1363, 2012.
- [6] R. Brendel, T. Dullweber, R. Peibst, C. Kranz, A. Merkle und D. Walter, „Breakdown of the efficiency gap to 29% based on experimental input data and modeling,“ *Progress in Photovoltaics: Research and Applications*, Bd. 20, Nr. 1, pp. n/a--n/a, 2015.
- [7] B. Fischer, Loss analysis of crystalline silicon solar cells using photoconductance and quantum efficiency measurements, Konstanz, 2003.
- [8] B. Thaidigsmann, a. Wolf, D. Biro, F. Ise und D. Freiburg, „Accurate determination of the IQE of screen printed silicon solar cells by accounting for the finite reflectance of metal contacts,“ in 24th European Photovoltaic Solar Energy Conference, 2009.
- [9] H. Holst, M. Winter, M. R. Vogt, M. R. Bothe, M. Köntges, R. Brendel und P. P. Altermatt, „Application of a New Ray Tracing Framework to the Analysis of Extended Regions in Si Solar Cell Modules,“ *Energy Procedia*, Nr. 38, pp. 86-93, 2013.
- [10] M. R. Vogt, H. Hahn, H. Holst, M. Winter, C. Schinke, M. Kontges, R. Brendel und P. P. and Altermatt, „Measurement of the Optical Constants of Soda-Lime Glasses in Dependence of Iron Content and Modeling of Iron-Related Power Losses in Crystalline Si Solar Cell Modules,“ *IEEE J. Photovoltaics*, Bd. vol. 6, p. 111–118, 2016.
- [11] C. Schinke, C. Peest, J. Schmidt, R. Brendel und K. V. M. W. M. Bothe, „Uncertainty analysis for the coefficient of band-to-band absorption of crystalline silicon,“ *AIP Adv*, Bd. 5, Nr. 6, p. 067168, 2015.
- [12] M. R. Vogt, „Development of Physical Models for the Simulation of Optical Properties of Solar Cell Modules,“ Phd thesis, German National Library of Science and Technology (TIB), 2015.
- [13] J. Levrat, C. Allebe, N. Badel, L. Barraud, M. Bonnet-Eymard, J. Champiaud, F. Debrot, A. Descoedres, A. Faes, A. Lachowicz, S. Nicolay, L. Sansonnens, C. Ballif, J. Geissbuhler, S. d. Wolf und M. Despeisse, „High-performance hetero-junction crystalline silicon photovoltaic technology,“ 2014 IEEE 40th Photovoltaic Specialist Conference (PVSC), pp. 1218-1222, 2014.
- [14] H. Serreze, „Optimizing solar cell performance by simultaneous consideration of grid pattern design and interconnect configuration,“ 13th Photovoltaic Specialists Conference, Bd. 1, pp. 609-614, 1978.
- [15] J. Müller, D. Hinken, S. Blankemeyer, H. Kohlenberg, U. Sonntag, K. Bothe, T. Dullweber, M. Kontges und R. Brendel, „Resistive Power Loss Analysis of PV Modules Made From Halved 15.6x15.6 cm² Silicon PERC Solar Cells With Efficiencies up to 20.0%,“ *IEEE Journal of Photovoltaics*, Bd. 5, Nr. 1, pp. 189-194, 2015.